Competition between recovery and recrystallization in two tungsten supplies according to ITER specifications

A. Durif, D. Piot, Marianne Richou, L. Gallais, M. Lemetais, Matthieu Lenci, M. Minissale, G. Kermouche

Noname manuscript No.
(will be inserted by the editor)

Competition between recovery and recrystallization in two tungsten supplies according to ITER specifications

Experimental assessment of initial state, recovery kinetics, and grain-boundary mobility, assisted by a mean-field model

A. DURIF · D. PIOT · M. RICHOU · L. GALLAIS · M. LEMETAIS · M. LENCI · M. MINISSALE · G.KERMOUCHE

Received: 05/08/2021 / Accepted: date

A. DURIF
CEA, IRFM, F-13108 Saint-Paul-Lez-Durance, France
Tel.: +33442253376
E-mail: alan.durif@cea.fr

D. PIOT
Mines Saint-Etienne, Univ Lyon, CNRS, UMR 5307 LGF, Centre SMS, F-42023 St-Etienne, France
E-mail: piot@emse.fr

M. RICHOU
CEA, IRFM, F-13108 Saint-Paul-Lez-Durance, France
E-mail: marianne.richou@cea.fr

L. GALAIS
Aix Marseille Univ, CNRS, Centrale Marseille, Institut Fresnel, Marseille, France
E-mail: laurent.gallais@centrale-marseille.fr

M. LEMETAIS
Mines Saint-Etienne, Univ Lyon, CNRS, UMR 5307 LGF, Centre SMS, F-42023 St-Etienne, France
E-mail: maxime.lemetais@emse.fr

M. LENCI
Mines Saint-Etienne, Univ Lyon, CNRS, UMR 5307 LGF, Centre SMS, F-42023 St-Etienne, France
E-mail: lenci@emse.fr

M. MINISSALE
Aix Marseille Univ, CNRS, PIIM, Marseille, France
E-mail: marco.minissale@univ-amu.fr

G. KERMOUCHE
Mines Saint-Etienne, Univ Lyon, CNRS, UMR 5307 LGF, Centre SMS, F-42023 St-Etienne, France
E-mail: kermouche@emse.fr

Abstract In thermonuclear fusion devices, tungsten, implemented as armour material of plasma facing components, is in direct contact with the plasma. Due to high heat flux (20 MW/m^2), a premature cracking can be observed in relation with the loss of tungsten mechanical properties. It is usually attributed to two competing restoration processes: recovery and recrystallization. A recent investigation on two tungsten supplies according to ITER specifications has highlighted that hardness abatement at high temperature leads to overestimate the recrystallization fraction, which may be a consequence of the significant contribution of recovery during annealing. The present article aims at investigating this phenomenon through the use of a dedicated mean field recrystallization model that, unlike JMAK models, accounts for physical parameters at the microstructure scale such as recovery parameter or grain boundary mobility. The methodology is applied on the two tungsten supplies for ITER. It allows discriminating, for the first time, the respective contributions of recovery and recrystallization to the macroscopic softening in the high temperature range [from 1450 to 1800°C] and annealing times [0–3500 s]. The approach has led to the conclusions that the two supplies merely differ from their initial (delivery) state through the stored energy, the initial recrystallized fraction and the grain size but not from intrinsic physical parameters such as recovery parameter or grain boundary mobility.

Keywords Tungsten · Softening · Recovery · Recrystallization · Mean-field model · ITER · Thermonuclear fusion

1 Introduction

Tungsten has been chosen for the ITER divertor and remains a potential candidate for future fusion reactors. This body-centered cubic structure refractory material has advantageous thermomechanical properties such as a high melting point (3400°C) and high thermal conductivity (173 W/(mK) at 20°C) [1]. It has also other advantages (low erosion, low thermal expansion, low retention of hydrogen isotopes, etc... [2]) but also some undesirables such as high Ductile to Brittle Transition Temperature [3] and high atomic number (Z=74) [4].

In view of operation budget, divertor lifetime is a concern for the future fusion reactors. The divertor lifetime is affected by material degradations under the different loadings including High Heat Flux (HHF) [5]. Resulting from rolling process, the tungsten microstructure changes during annealing at high temperature driven by lattice stored energy in the material. During annealing, two competing mechanisms might be involved: recovery (decrease of dislocation density and other crystal defects) and recrystallization (nucleation and nuclei growth) [6] that both induce a macroscopic softening that can be revealed using hardness tests. For tungsten manufactured according to the ITER specifications, recovery is shown to be the main mechanism at the beginning of the heat treatments [7]. Then recrystallization prevails. Richou et al [8] have shown that recrystallization kinetics strongly depend on the supplier by

performing high temperature annealing on two tungsten materials, that both fulfil the ITER specifications. They also have highlighted that hardness abatement at high temperature leads to overestimate the recrystallization fraction, which may be a consequence of the significant contribution of recovery during annealing. All of these results pointed out the key-role of the tungsten-based plasma-facing materials microstructure on recrystallization and thus on divertor durability. There is thus a strong need to develop models dedicated to the investigation of tungsten recovery/recrystallization at high temperature for thermonuclear fusion applications. Such models could even be used to determine through a retro engineering approach the ideal tungsten microstructure for armoured plasma facing component lifetime.

Four main approaches exist to model static recrystallization, (I) The analytic and phenomenological Johnson- Mehl-Avrami-Kolmogorov (JMAK) model [9,10] is often employed and was largely developed by Humphreys [6] in the literature. This model proposes a unified description of these two (recovery/recrystallization) mechanisms considering constant nucleation rate and spherical nuclei once recrystallization starts. Applied to softening kinetics, this model describes the impact of recovery and recrystallization assuming that the rates of new grain nucleation and growth of recrystallized grains are constant. Up to date experimental studies, resulted in the identification of JMAK kinetics for several tungsten grades according to Vickers experimental data. JMAK kinetics were identified up to $1400°C$ [7,11,12,14–16] using oven and at higher temperatures (up to $1800°C$) [8] using a high power laser facility [17]. More computationally complex methods taking into account material physics can be considered such as (II) probabilistic methods (Monte-Carlo [13] [18], Cellular Automata [19] [20]) or (III) methods based on microstructure meshing (Vertex [21], Phase-field [22] or level set method [23]). In between the first phenomenological and more complex approaches, there is (IV) the mean-field approach [24,25]. Up to now, mean field approach was used by Mannheim to model tungsten recrystallization under neutron irradiation [26,27]. In the study performed by Richou et al [8], Electron Back Scattered Diffraction (EBSD) measurements revealed that the recrystallization fraction (X) is likely overestimated by hardness measurements. An unified description of recovery/recrystallization mechanisms using JMAK kinetics may be not sufficient as neither dislocation densities nor grain mobilities are direct constitutive parameters in this kind of macroscopic model [9,10]. An approach based upon a mean-field model for recovery and recrystallization is an alternative way to account for physical parameters such as dislocation density (ρ) and grain-boundary mobility (M) in order to deeper explore the balance between recovery and recrystallization [24,25,28]. A mean field description consists in the modelling of the interaction of a grain with an equivalent homogeneous matrix whose properties are the average properties of all the grains [29]. The size and dislocation density of each grain are predicted by evolution equations. Two main mechanisms contribute to these evolutions: (i) Grain-boundary migration: the stored energy difference is the main driving force (pressure) of the migration ($\Delta\Theta$). With the grain boundary migration rate (V)[6]:

$$V = M\Delta\Theta \tag{1}$$

Positive driving force leads to an increase in size of the grain and negative driving force leads to a decrease in size. Note that the grain-boundary mobility (M) depends on temperature by thermal activation. (ii) Static Recovery: the rate of dislocation density depends on dislocation density and temperature. Static recovery summarizes all thermally activated mechanisms by which dislocations annihilate and rearrange themselves into more stable configurations. Such mechanisms lead to a decrease of dislocation density ($\rho(t)$) over the annealing time. Most of time, the decrease of dislocation density laws are empirically established and chosen under isothermal conditions [28] such as:

$$\frac{d\rho(t)}{dt} = -r\rho(t) \tag{2}$$

With r (s^{-1}), the recovery parameter which is a second key thermally-activated parameter within a mean field approach. To sum up, input data of mean field models are the physically-based parameters related to recovery and recrystallization and the initial microstructural state representative of the tungsten production history (deformation, heat treatment, etc), that can be described through the stored energy -i.e.dislocation density, ... - , the grain size distribution,the crystallographic texture and the initial fraction of nuclei. Given a prescribed thermal history, output data are recovery and recrystallization kinetics, average grain size and hardness. Refined methodologies accounting for grain topology [28] could even allow predicting grain size distribution, therefore bridging the step between mean field and full field models.

Although recrystallisation mean field approaches have been developed for years, it has barely been used to investigate tungsten restoration kinetics in the framework of thermonuclear fusion application. Therefore the main goal of this paper is not to develop an original model for recrystallization. But it is rather to assess the potential of a mean field approach to get a better understanding of the effect of the initial microstructural state on recovery/ recrystallization kinetics, which cannot be accurately described through conventional JMAK models. In this paper, the mean field approach is applied on the two tungsten materials investigated by Richou et al [8], which fulfil the ITER specifications. They are referenced as type A and type B materials since their production history remain the property of the supplier and cannot be disclosed in this paper. However their microstructure that strongly differ in terms of grain size, stored energy and initial fraction of nuclei are known through EBSD measurements. Mean-field parameters and kinetics are identified based on the softening fractions (X_H) and X measured experimentally for both materials. In section 2, the parameter for recovery is identified in order to discriminate the respective contribution of recovery and recrystallization in the final softening kinetics. Section 3 then deals with the characterization of the initial state, the model for recrystallization kinetics, and the evaluation of the grain-boundary mobility.

2 Recovery parameter

2.1 Raw data

Material	type A	type B
Hv_0	$435 \pm 7 Hv_{10}$	$427 \pm 8 Hv_{10}$
H_{recr}	$359 \pm 6 Hv_{10}$	$361 \pm 4 Hv_{10}$
X_{init}	0.15	0.07

Table 1 Parameters related to types A and B materials [8]

Materials used for this study are, so called, type A and B tungsten materials in [8]. No information about the manufacturing process of these two materials complying with the tungsten ITER specifications, provided by two different suppliers was communicated.

Richou et al results [8], revealed that the initial microstructure of types A and B materials are composed of grains (highly deformed due to the manufacturing process) and nuclei (recrystallized new grains) at the initial as-received state. It was notably highlighted that the recrystallization fraction of the as-received material (X_{init}) is equal to 15 % and 7 % for types A and B materials respectively. In parallel, the hardness of the as-received state (Hv_0) and fully recrystallized (H_{recr}, Hv at $X = 1$) has been measured by standard (load of 10 kgf) Vickers indentation. As a reminder, table 1 summarizes these results for types A and B materials.

EBSD measurements were performed according to the procedure set in [8] on annealed samples giving the possibility to compare the related X to the measured average hardness. As a reminder, samples were annealed by the use of the experimental device described in [17]. Figures 1 and 2 present these results. They show the evolution of hardness and X over annealing time at $1450°C$, $1500°C$, $1550°C$ and $1600°C$ for type A material and at $1500°C$, $1600°C$, $1700°C$ and $1800°C$ for type B material respectively.

It can be noted that recrystallization do not lead to the entire hardness decrease. Indeed, as an example, the minimum hardness for type A material is obtained after 3000 s at $1550°C$ while tungsten is not fully recrystallized ($X = 0.71$). Similar trends are observed in type B material.

In order to quantify the respective contribution of recovery and recrystallization in the resulting softening kinetics, subsection 2.2 aims at presenting a method for estimating the recovery parameter from these available data.

2.2 Method

In the present case, the material is assumed to be a polycrystal with grains that are recrystallized or unrecrystallized. For investigating recovery, the focus is on the average dislocation density among only the unrecrystallized grains.

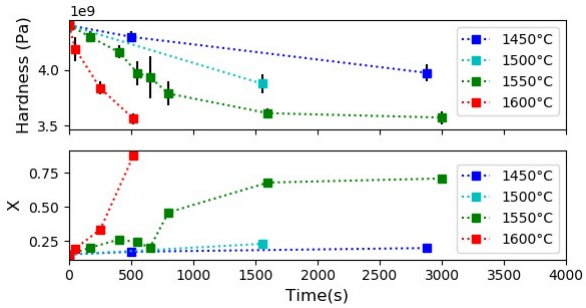

Fig. 1 Hardness measurements and X (estimated by EBSD) evolution over annealing time at $1450°C$, $1500°C$, $1550°C$ and $1600°C$ for type A material. The dotted lines are only for guiding eyes

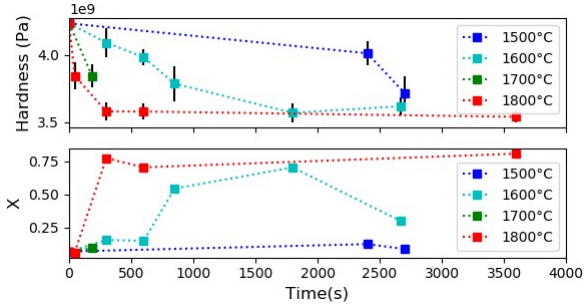

Fig. 2 Hardness measurements and X (estimated by EBSD) evolution over annealing time at $1500°C$, $1600°C$, $1700°C$ and $1800°C$ for type B material. The dotted lines are only for guiding eyes

Once integrated, the first order ordinary differential equation (2) gives:

$$\rho(t) = \rho_{def} \exp(-rt) \tag{3}$$

$$-\ln(\frac{\rho(t)}{\rho_{def}}) = rt \tag{4}$$

where ρ_{def} corresponds to the dislocation density of the initial unrecrystallized (deformed) grains ($X = 0$).

To identify r, the dislocation density, $\rho(t)$, is linked to the material Vickers hardness (Hv) through the Tabor relation [30]:

$$Hv(t) = c\sigma^y(t) \tag{5}$$

in which σ^y corresponds to the macroscopic yield stress (in MPa) and c is the Tabor constant having a value close to 3 for metals [30,31]. Here, c is set to 3.

In the present article, the dislocation density of the fully recrystallized material is assumed to be 0. Consequently, the σ^y is expressed as function of H_{recr} and dislocation density $\rho(t)$:

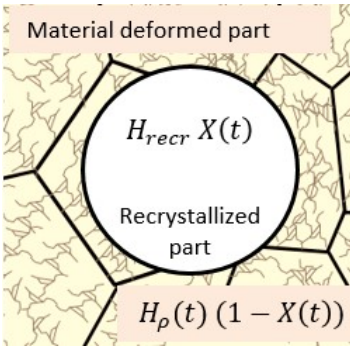

Fig. 3 Schematic view of hardness related to the unrecrystallized (deformed) material ($H\rho$) and the recrystallized material (H_{recr})

$$\sigma^y(t) = \frac{H_{recr}}{c} + M'\alpha\mu b_g\sqrt{\rho(t)} \tag{6}$$

In which:
-M': defines the Taylor factor
-α: a material constant
-$M'\alpha$ is assumed to be 1 after [32,31]
-μ: the tungsten shear modulus (Pa) taken at room temperature [1]
-b_g: Magnitude of Burgers vector: $2.73.10^{-10}$m [32]

The softening fraction (X_H) is expressed as a function of the current hardness ($Hv(t)$), the initial hardness of unrecrystallized grains (H_{def}, Hv at $X = 0$) and the hardness of the fully recrystallized material (H_{recr}, Hv at $X = 1$) as follow:

$$X_H(t) = \frac{H_{def} - H_v(t)}{H_{def} - H_{recr}} \tag{7}$$

With:

$$H_{def} = \frac{Hv_0 - X_{init}H_{recr}}{1 - X_{init}} \tag{8}$$

According to figure 3, the following mixture rule gives the macroscopic material hardness (Hv) [24]:

$$H_v(t) = H_{recr}X(t) + H_\rho(t)(1 - X(t)) \tag{9}$$

Where H_ρ corresponds to the current hardness of the material remaining unrecrystallized, and combining equations 5, 6, it results:

$$H_\rho(t) = H_{recr} + 3\mu b_g\sqrt{\rho(t)} \tag{10}$$

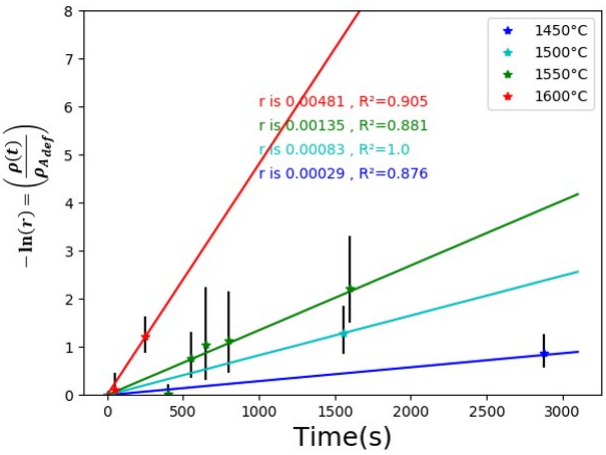

Fig. 4 Recovery parameter (r) for type A material. With r corresponding to the slope

In this manner:

$$H_v(t) = H_{recr} + 3\mu b_g \sqrt{\rho(t)}(1 - X(t)) \tag{11}$$

Combining equations 11 and 7:

$$\rho(t) = \frac{\rho_{def}[1 - X_H(t)]^2}{[1 - X(t)]^2} \tag{12}$$

Equation 12 gives the direct expression of $\rho(t)$ in terms of X and X_H. The following linear regression equivalent to equation 4 leads to determine r from the collected raw data of X and X_H (figures 1 and 2):

$$-ln\left(\frac{[1 - X_H(t)]^2}{[1 - X(t)]^2}\right) = rt \tag{13}$$

It is worth to note that this regression is not affected by any uncertainty related to the identification of ρ_{def}. Through this method, r is defined for each annealing temperature and material. Once r determined over temperature range, evolution of this parameter is given in form of Arrhenius function to characterize the material activation energy (Q) for the recovery.

Logarithm formulation tends toward infinity and leads to undefinable error bars once X_H is in the neighbourhood of one which do not allow proper estimation of the error bars related to the experimental point. In that way, this point is not taken into account to fit equation 13. In the following results subsection, r is determined if a minimum of two experimental points are available.

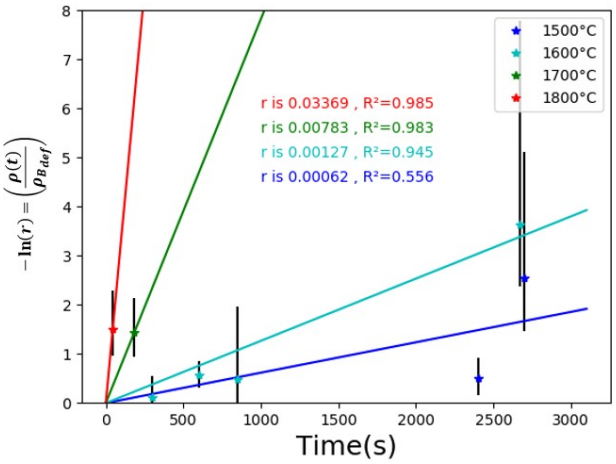

Fig. 5 Recovery parameter (r) for type B material. With r corresponding to the slope

2.3 Results

According to these results, equations 8 and 11 give $H_{A_{def}} = 449\,Hv_{10}$ and $\rho_{A_{def}} = 4.90 \times 10^{13}\,/m^2$ for material type A and $H_{B_{def}} = 432\,Hv_{10}$ and $\rho_{B_{def}} = 3.02 \times 10^{13}\,/m^2$ for type B material. It can be noted that $\rho_{B_{def}}$ is 38% lower than $\rho_{A_{def}}$.

Using equation 13, r is estimated for type A material, over the explored temperature range ($1450°C$ – $1600°C$) (figure 4).

In the same way, r is estimated for material B, over the explored temperature range ($1500°C$ – $1800°C$) (figure 5). For both materials, determination coefficients (R^2) are always greater than 0.87 (apart type B at $1500°C$, the last two points appearing doubtful); they do not have meaning when the regression is fitted on only two points.

2.4 Discussions

Figure 6 (a) illustrates the temperature dependence of r respectful to the types A and B supplies and depicts the regression of Arrhenius law to assess the corresponding apparent activation energy (Q). Obtained results highlight that Q are equivalent for type A ($Q_A = 522\,kJ/mol$) and type B ($Q_B = 414\,kJ/mol$) materials. As A and B supplies are pure tungsten (99.94%), it may be assumed that activation energy can also be fitted based on the whole experimental points (material A and B, green fit). The resulting activation energy is called Q_{A+B}. Q_{A+B} obtained is equal to $391\,kJ/mol$. This result is consistent with the activation energy of $360\,kJ/mol$ obtained by A. Alfonso et al for another tungsten (W90) [14].

Assuming identical chemical composition for material A, B and W90, the only difference between these tungsten grades is attributed to the manufac-

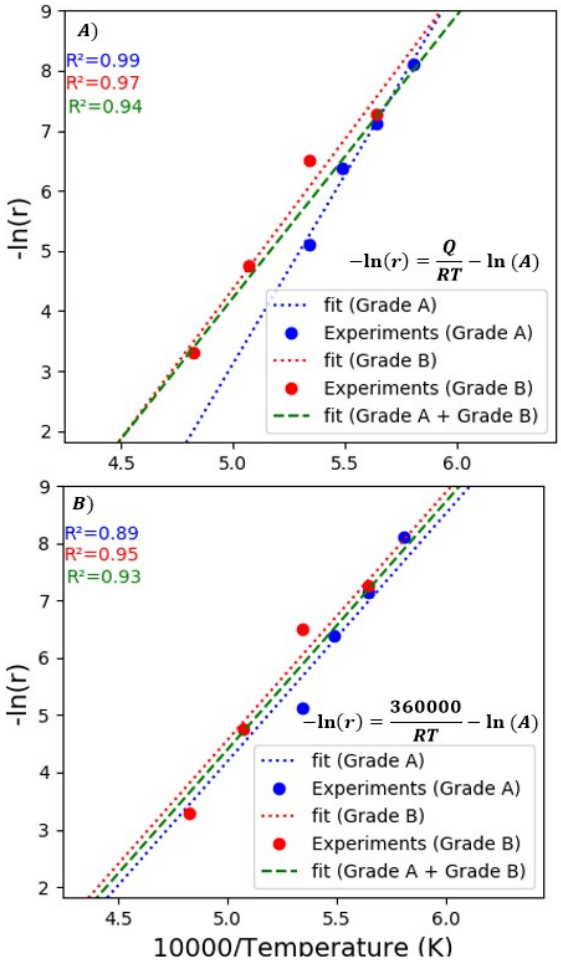

Fig. 6 a) Activation energy (Q) identified for material A, B and A+B by using least square method to determine A and Q. b) Linear regression for material A, B, and A+B by constraining Q to 360 kJ/mol[14].

turing process. Transformation processes seem not to play a significant role on the activation energy of recovery (figure 6, b) whereas they naturally influence X_{init} (15 % for A, 7 % for B and 0 % for W90), the initial dislocation density ($4.90 \times 10^{13}\,/m^2$ for A and $3.02 \times 10^{13}\,/m^2$ for B) and the initial grain and nucleus size distributions (highlighted previously in [8]). In the following, r parameter obtained from experimental points from types A and B materials (green curve, figure 6 (a)) is used as input data in the mean field model.

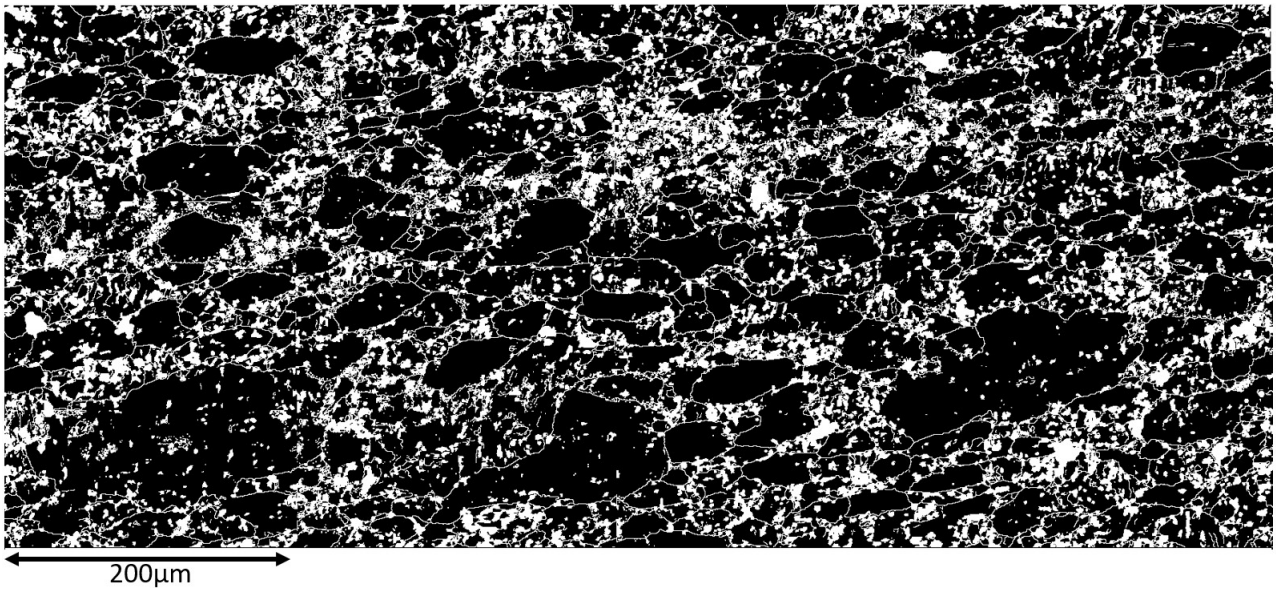

Fig. 7 EBSD maps obtained on as-received sample for the type A material (in the plan normal to the normal direction). Initial deformed grains are displayed in black and nuclei in white color.

3 Recrystallization kinetics and grain-boundary mobility

3.1 Description of the initial state (grain population)

In the mean field model [29,28], the material microstructure is described by the grain size distribution and the dislocation densities representative of the energy stored in the material. Initial deformed (unrecrystallized) grains and nuclei (recrystallized grains) distributions are then used as input data in such model. It is consequently needed to identify properly these initial distributions. The size distributions of initial nuclei and deformed grains are identified based on EBSD maps. First, identified grains (deformed grain or nucleus) are classified. If the internal misorientation angle in a detected grain exceeds the minimum angle to define a substructure (2°), the detected grain is defined as deformed one. The remaining detected grains are defined as nuclei.

Second, an image processing is performed via the use of ImageJ software to obtain the size of each grain. Assuming spherical grains, equivalent radius (R) can be obtained for each deformed grain and nucleus.

Log-normal like functions are fitted based on the use of the least squares method to identify nucleus and initial deformed grain radius distributions. The use of the standard log-normal functions (equation 14) did not allow consistent fit of nucleus and initial deformed grain radius distributions. In that way, x in equation 14, corresponds to the logarithm of radius ($x = ln(R_i)$).

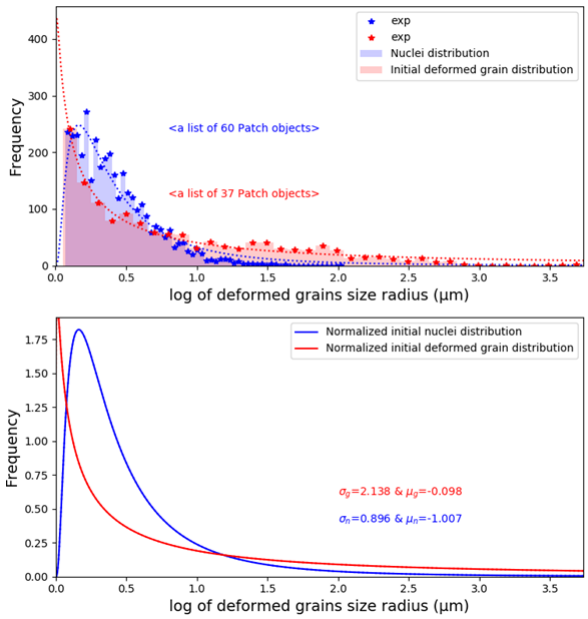

Fig. 8 (up) Histograms distributions obtained for type A material. (Down) Related normalized distributions identified for type A material.

$$f(x) = \frac{1}{\sigma_n x\sqrt{2\pi}} exp^{(-\frac{(ln(x)-\mu_n)^2}{2.\sigma_n^2})} \tag{14}$$

The number of patches (N_{patch}) which constitute distribution histogram of deformed grains or nuclei is defined based on total number of detected deformed grains ($N_{defgrain}$) or nuclei (N_{nuclei}) respectively as:

$$N_{patch} = \sqrt{N_{defgrain}} \tag{15}$$

It is important to note that log-normal distributions are not fitted on the smallest grain region. Indeed, due to EBSD step (0.5 μm)and EBSD indexation rate, a filter (F) is applied to exclude small surface area particles. F is set to 3 μm^2, which means that all detected grain area less than 3 μm^2 are not accounted for the histogram distribution to fit the log-normal function.

Used as input data, these distributions need to be normalized to 1. Log-normal function considering $x = ln(R_i)$ leads to an overestimation of large grains. To be relevant regarding the EBSD observations, the maximum grain radius generated during random selection cannot be higher than the maximum grain/nucleus sizes detected (by EBSD). If higher radius is generated during the random selection, new selection is performed.

Based on EBSD maps (figure 7) and the previous identification method, the figure 8 (up) shows the initial (t=0) histograms of distributions of nuclei (blue) and deformed grains (red) for type A material.

	Initial def. grain	Initial nuclei
e^u	0.91	0.37
Median (e^{e^u}, μm)	2.47	1.44
Standard dev. (σ)	2.14	0.90

Table 2 Parameters related to initial normalized distributions for type A material

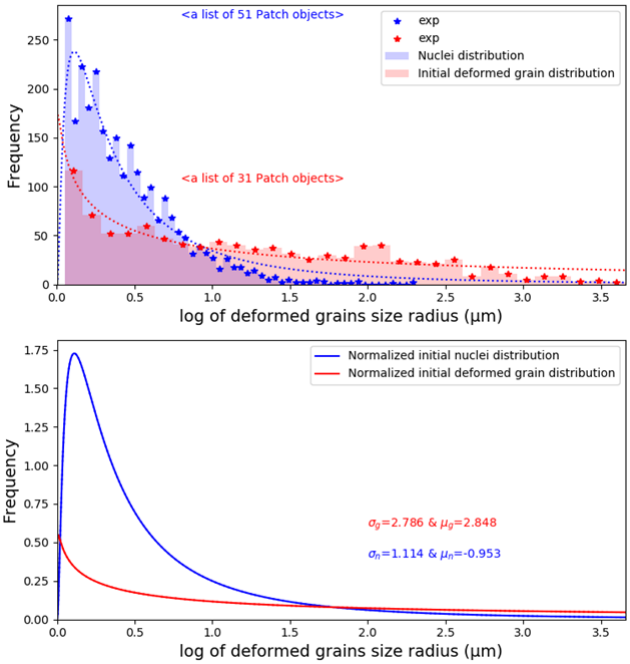

Fig. 9 (up) Histograms distributions obtained for type B material. (Down)Related normalized distributions identified for type B material.

The larger EBSD map collected to characterize the initial microstructure state of material A is used (composed of 16 stitched small maps, figure 7). The presented histograms take into account nuclei and initial deformed grains with radius up to 7.6 μm and 42.3 μm respectively. N_{patch} is displayed directly on the histograms. This figure also presents the log-normal fitted functions. The number of coarse initial deformed grain is slightly overestimated for grains (from ln(3.0) μm) and nuclei (from ln(1.0) μm). Finally, figure 8(down) displays the normalized log-normal distributions obtained and their related parameters.

The table 2 gives physical interpretations of the obtained log-normal parameters (median and standard-deviation). As expected in the initial state, unrecrystallized grains are relatively coarse and recrystallized grains (nuclei) are finer.

Due to smaller EBSD maps obtained for type B material, log-normal size distributions are identified based on several EBSD maps achieved on as-

	Initial def. grain	Initial nuclei
e^u	17.25	0.39
Median (e^{e^u}, μm)	31×10^6	1.47
Standard dev. (σ)	2.78	1.11

Table 3 Parameters related to initial normalized distributions for type B material

received samples. Figure 9 (up) shows the initial histograms distributions of nuclei (blue) and deformed grain (red) for material B. The presented histograms take into account nuclei and initial deformed grains with radius up to 10.1 μm and 38.9 μm which are the maximum particle size detected respectively. The number of patches is displayed directly on the histograms. Figure 9 (down) displays the normalized log-normal distributions obtained and attached parameters. The table 3 gives related log-normal parameters obtained. A huge median is obtained without physical meaning, it is due to the very large spread of such a log-log-normal distribution and related to the overestimation of the density function at large radius above 20 μm ($> ln(3.0)$).

3.2 Mean field model

In the mean field model, the material microstructure is described through the grain size distribution and the dislocation densities representative of the energy stored in the material. Each grain interacts with an equivalent homogeneous matrix (EHM) having the material average microstructure property. Spherical grains are assumed. Grain size and dislocation density are considered as state variables. Consequently, grain "i" is characterized by its radius (R_i) and its dislocation density (ρ_i) which is assumed to be homogeneous within the grain. Since X_{init} is different to zero for types A and B material [8], nucleation process occurred before performing annealing. Consequently, nucleation is not taken into account in the mean field model.

The algorithm of mean field model is presented in figure 10. Computational information are given in appendix A

The evolution of R_i and ρ_i are estimated at each time increment according to the models for recovery and grain-boundary migration. The latter is driven by the difference in dislocation density between the considered grain "i" and the current equivalent homogeneous medium. This is taken into account through the following grain-boundary migration constitutive equation [28,29]:

$$\frac{dR_i(t)}{dt} = M\tau(\bar{\rho}(t) - \rho_i(t)) \tag{16}$$

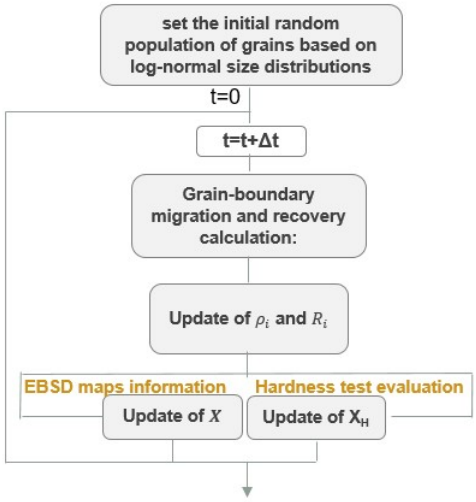

Fig. 10 The mean field model algorithm

With:
-M: Grain-boundary mobility ($T°$ dependent)(m/(Pa.s))
-τ: Line energy of dislocations ($T°$ dependent)
-$\overline{\rho}$: Average dislocation density within all grains (m^{-2})
-ρ_i: Dislocation density of the grain 'i' (m^{-2})
-R_i: Radius of the grain 'i' (m)

When $\rho_i(t) < \overline{\rho}(t)$ the radius of grain "i" increases (nucleus)

When $\rho_i(t) > \overline{\rho}(t)$ the radius of grain "i" decreases until the deformed grain disappears.

According to this equation, once the material is fully softened ($X_H = 1$), the grain size does not increase anymore. The present model does not take into account the grain growth so it is dedicated to short annealing.

Boundary mobility (M) is material and temperature dependent. As factor of driving force, this parameter plays major role by giving the grain-boundary velocity. The method used to identify this parameter is discussed at the end of the subsection.

Equation 16 introduces τ which corresponds to the dislocations line energy so that the product $\tau\rho$ correspond to the stored energy:

$$\tau(Pa.m^2) = \frac{\mu b_g^2}{2} \tag{17}$$

With:
-μ: Tungsten shear modulus (Pa) considered at the annealing temperature according to the equation 18
-b_g: Magnitude of Burgers vector: $2.73.10^{-10}m$ [32]

$$\mu(Pa) = \frac{E}{2(1+\nu)} \tag{18}$$

With:
-E: Tungsten Young modulus estimated at the annealing temperature (T) based on the following approximation: $(397.903 - (0.00231 * T) - 0.000027 * T^2) * 10^9$Pa [1]
-ν: Poisson's ratio (0.29) [1]

To ensure volume conservation over numerical annealing, $\overline{\rho}(t)$ is defined as follow [29]:

$$\bar{\rho}(t) = \frac{\sum_1^n \rho_i(t) R_i^2(t)}{\sum_1^n R_i^2(t)} \tag{19}$$

Over the softening process, deformed grains will shrink then disappear. To ensure volume conservation, the residual volume of disappearing grains is redistributed in equal part to each nucleus.

Considering the whole population of grains into equation 11, the evolution of the material hardness can be easily computed at each time by:

$$Hv(t) = H_{recr} + 3\mu b_g \frac{\sum_1^n R_i(t)^3 \sqrt{\rho_i(t)}}{\sum_1^n R_i^3(t)} \tag{20}$$

Finally, the recrystallization fraction X is computed as the ratio of the total volume of recrystallized grains (V_{nuclei}) over the whole volume (deformed grain + nucleus, V_{total}):

$$X(t) = \frac{V_{nuclei}(t)}{V_{total}} \tag{21}$$

The model is initialized with a population of unrecrystallized grains randomly selected as specified in section 3.1. In the following, this population is fixed to contain 100 grains expecting a priori to be enough representatives. The volume of initial deformed grains (V_{def}) is firstly calculated. Then based on a simple mixture law (equation 22, [24]) nuclei are randomly selected for initialization according to section 3.1 up to attain the expected total volume of nuclei ($V_{nuclei}(t_0)$), where:

$$V_{nuclei}(t_0) = \frac{X_{init}}{1 - X_{init}} V_{def} \tag{22}$$

M (equation 16) has to be determined for each annealing temperature. In this study, M is identified according to X_H and X. For this, M is calculated by the use of a gradient algorithm to provide the minimum of quadratics errors (QE_{X-X_H}) related to X_H and X (equation 23) between the model output and the experimental X_H and X. In that way, identical weight are given to the quadratic errors obtained on each kinetics (X_H and X).

type A	M (m/(Pa.s))
$1450°C$	$(3.84 \pm 0.219) \times 10^{-15}$
$1500°C$	$(8.56 \pm 0.513) \times 10^{-15}$
$1550°C$	$(3.26 \pm 0.248) \times 10^{-14}$
$1600°C$	$(1.42 \pm 0.161) \times 10^{-13}$
type B	
$1500°C$	$(7.04 \pm 0.631) \times 10^{-15}$
$1600°C$	$(9.76 \pm 0.740) \times 10^{-14}$
$1700°C$	$(6.84 \pm 0.744) \times 10^{-14}$
$1800°C$	$(1.82 \pm 0.152) \times 10^{-12}$

Table 4 M obtained for types A and B materials according to X and X_H. The confidence intervals correspond to the standard deviation estimated from the 5 runs.

$$QE_{X-X_H} = \frac{XHQE}{2} + \frac{XQE}{2} \tag{23}$$

In order to give M approximation taking into account the influence of the initial population of grains, mean field model is run 5 times based on 5 random populations of 100 initial unrecrystallized (deformed)grains.

3.3 Results

Table 4 (up) summarizes the M values obtained for the type A material. As expected from thermal activation, one can conclude that the mobility of grain boundaries in type A increases when temperature increases from $3.84 \times 10^{-15} \pm 0.219\, m/(Pa.s)$ at $1450°C$ to $1.42 \times 10^{-13} \pm 0.161\, m/(Pa.s)$ at $1600°C$.

By the same way, table 4 (down) is for type B material. It is highlighted again that M is thermally activated from $7.04 \times 10^{-15} \pm 0.631\, m/(Pa.s)$ at $1500°C$ to $1.82 \times 10^{-12} \pm 0.152\, m/(Pa.s)$ at $1800°C$.

The variation of M vs. temperature for both types is plotted as an Arrhenius graph in 11. As the coefficient of determination always appears greater than 0.84, the Arrhenius chart allows to determine the apparent activation energy of M. For type A material, it is $Q_{MA} = 467\, kJ/mol$ and $Q_{MB} = 364\, kJ/mol$ for type B material.

The output data of the model lead to explore the competition between recovery and recrystallization allowing to quantify their respective impact on softening kinetics. Figures 12 and 13 depict the computed kinetics of X_H and X for types A and B respectively. Experimental points related to X_H (from hardness) and X (from EBSD) are also displayed. It is worth to note that all these kinetics appear consistently reliable regarding enough small quadratic errors.

3.4 Discussions

The present article provides quantitative data about some physical parameters for types A and B materials like the recovery parameter r and the grain-

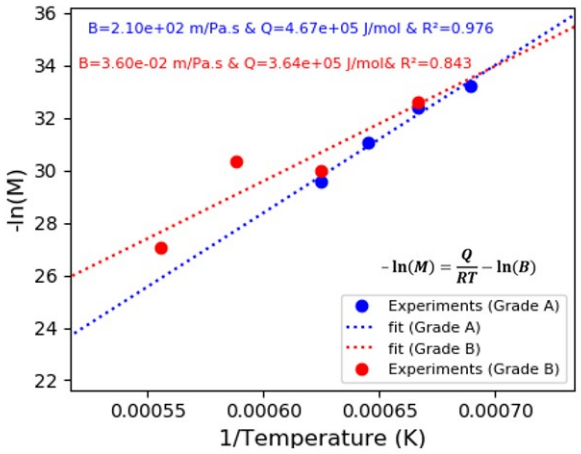

Fig. 11 Arrhenius plot of the grain-boundary mobility M for types A and B materials as fitted on both X_H and X

boundary mobility M and their apparent activation energy or differences in the initial (delivery) states of both types due to the details of their processing routes. Especially each type mainly departs from the other by the initial recrystallization fraction, the initial dislocation density of the unrecrystallized grains, the distribution of grain size for both recrystallized and unrecrystallized grains. The determination of the apparent M and r activation energies give the opportunity to predict the softening and recrystallization kinetics at an uninvestigated temperature.

Although the uncertainties related to the experimental means can be important (up to 40 %) on X_H, the general coherence of the modeling makes it possible to discuss on kinetics curves. Kinetics highlight that softening and recrystallization processes are involved in different manner during the annealing which proves that both recrystallization and softening processes have to be separately considered. For example, outputs of mean field model reveal that type B material is 60 % softened after 4000 s at $1500°C$ while material is 17 % recrystallized.

In order to position this work to the literature, obtained Mean Field approach softening kinetics (MF) are compared to the JMAK ones. For that, (i) JMAK kinetics are fitted based on the MF (JMAK_MF) and (ii) JMAK kinetics are fitted based on experimental data (JMAK_exp). For both, kinetics are fitted by adjusting, using least-square regression analysis, the two JMAK parameters, b and n (JMAK equation is given as a reminder in appendix B, equation 5). In our case, there is already a non-zero softening fraction at t=0, as if the material had already undergone an equivalent holding time (t_{eqh}) at the annealing temperature. To take it into account, t_{eqh} have been introduced in the JMAK equation so that the softening fraction at t = 0 is the one resulting from the actual previous history of the material (0.155 and 0.065 for type

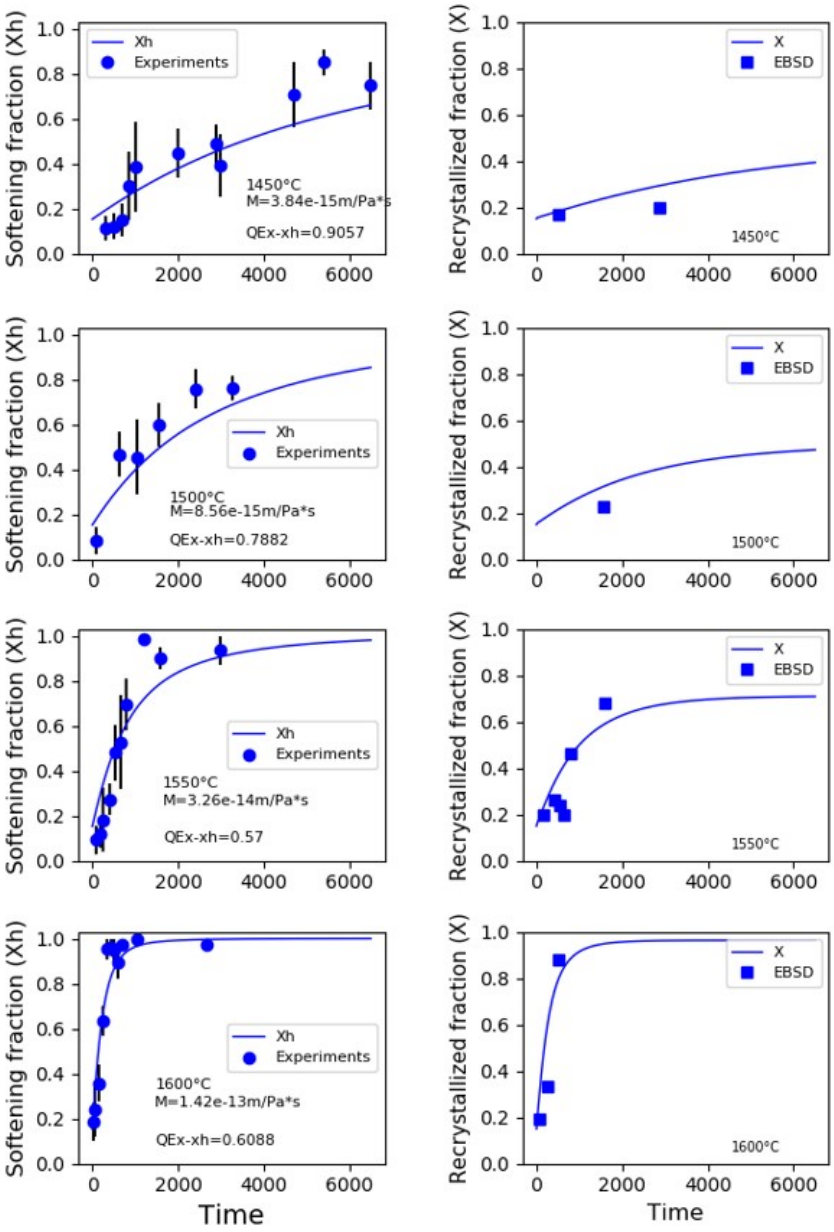

Fig. 12 Softening and recrystallization kinetics obtained for type A material based on X_H and X identification

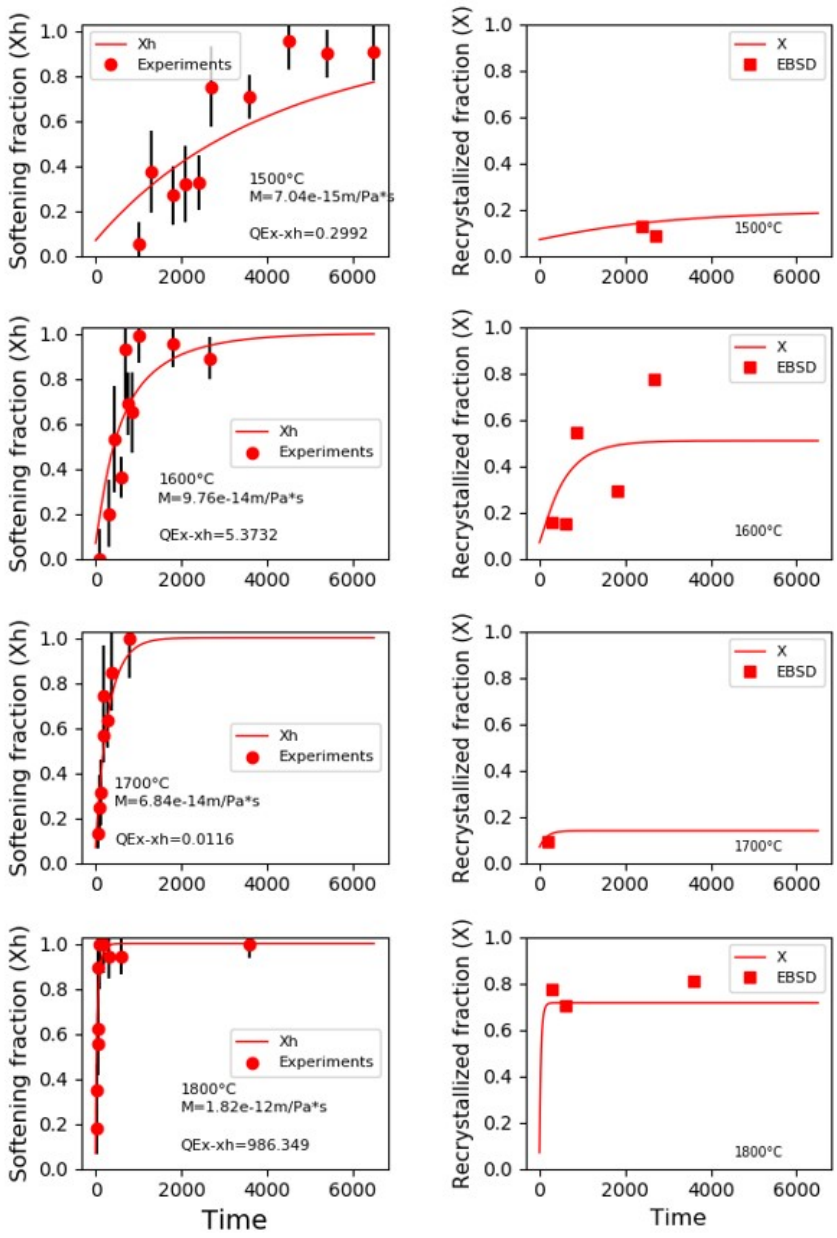

Fig. 13 Softening and recrystallization kinetics obtained for type B material based on X_H and X identification

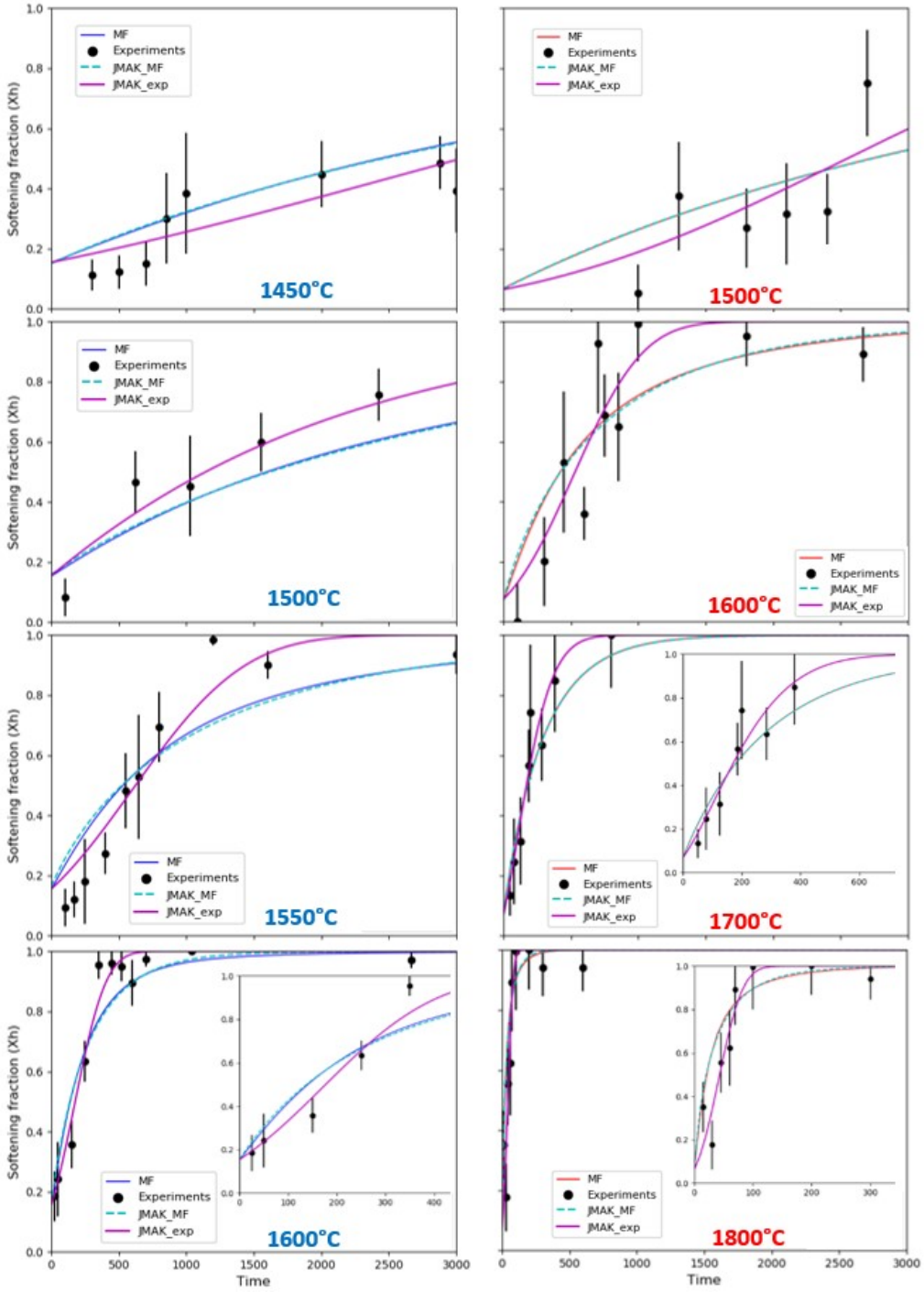

Fig. 14 Qualitative comparison of the softening kinetics (MF, JMAK_MF and JMAK_exp) obtained for type A (a) and type B (b) materials at $1600°C$.

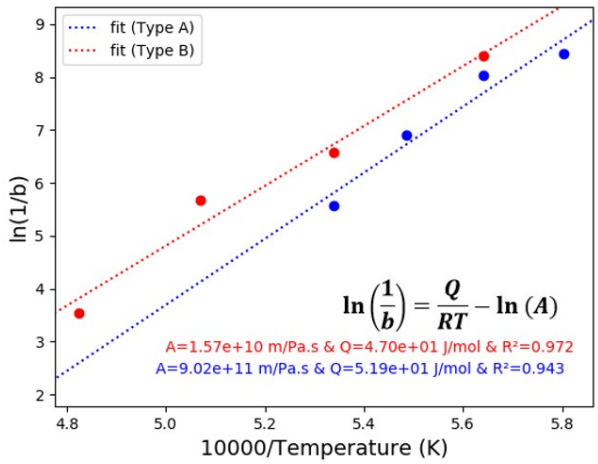

Fig. 15 Arrhenius plot of the JMAK parameter b for types A and B materials related to the JMAK_MF kinetics.

A and B respectively). Figure 14 gives qualitative comparison of all kinetics obtained for type A (left) and B (right) materials. JMAK_MF and JMAK_exp kinetics are close to the MF ones. JMAK_MF fit well the MF kinetics.

JMAK parameters obtained for kinetics related to JMAK_MF are summarized table 5. The variation of the thermo-dependent parameter b vs. temperature for both types is plotted as an Arrhenius graph in figure 15. The determination coefficients appear greater than 0.94, which give the opportunity to determine the apparent activation energy of b. For type A material, it is $b_A = 519\,kJ/mol$ and $b_B = 470\,kJ/mol$ for type B material. It can be noted that Avrami exponent can be considered as constant for type A (0.85 ± 0.06) and type B (0.87 ± 0.09).

Presented in appendix B, JMAK parameters obtained for JMAK_exp (7)allow a direct comparison with JMAK_MF parameters. The Arrhenius graph presented figure 16 highlight the variation of b over the temperature range (for JMAK_exp kinetics). The determination coefficients are greater than 0.93 and the b apparent activation energy is $b_A = 442\,kJ/mol$ for type A material and $b_B = 417\,kJ/mol$ for type B material. Related Avrami exponent may be considered as constant for type A (2.35 ± 0.92) and B (2.64 ± 0.63). It can be noted that n is close to 3 which can be compared to the exponent 3 presented by Humphreys et al assuming satured nucleation sites [6]. Parameters obtained for types A material at $1450°C$ can be directly compared to the ones obtained at same temperature by Shah in [11]. b obtained here is one order of magnitude lower and n is twice lower. This unique point of comparison cannot discredit the results obtained here or presented in literature. Difference may lie with the chemical impurities present in the material or with the manufacturing process used. It was notably shown by Wang in [33] that the manufacturing process plays significant role on the final JMAK kinetics.

type A	b	n	$t_{eqh}(s)$
$1450°C$	2.16×10^{-4}	0.88	600
$1500°C$	3.23×10^{-4}	0.84	385
$1550°C$	1.00×10^{-3}	0.78	112
$1600°C$	3.80×10^{-3}	0.91	37
type B			
$1500°C$	2.26×10^{-4}	0.93	250
$1600°C$	1.40×10^{-3}	0.83	30
$1700°C$	3.40×10^{-3}	0.96	19
$1800°C$	2.90×10^{-2}	0.76	1.1

Table 5 JMAK parameters related to JMAK_MF obtained for types A and B materials.Mean field model was run 1 times based on a random populations of 100 initial unrecrystallized (deformed) grains. It is thus important to note that deviations might be obtained in the order of 7 % and 2 % for parameters b and n respectively

	Time (s) to reach $X_H = 50\%$ ($t_{X=50\%}$)		
type A	MF	JMAK_MF	JMAK_exp
$1450°C$	2433	2460	3037
$1500°C$	1596	1617	1143
$1550°C$	531	522	623
$1600°C$	140	139	177
type B			
$1500°C$	2725	2734	2548
$1600°C$	421	425	532
$1700°C$	180	180	171
$1800°C$	22	20	43

Table 6 Time to reach $X_H = 50\%$ ($t_{X=50\%}$) for types A and B materials. Mean field model was run 1 times based on a random populations of 100 initial unrecrystallized (deformed)grains to obtained this results. It is thus important to note that deviations might be obtained in the order of 10% for on MF and JMAK_MF in case of rerun

Finally, JMAK parameters deviations do not play significant role on the final results compare to the kinetics obtained by the mean field approach. Table 6 presents for each kinetics, the time needed to reach 50 % softening ($t_{X=50\%}$) which allows a quantitative comparison of all kinetics obtained at each temperature. Maximum deviation between by JMAK_exp and MF kinetics is less than 29 % for type A and 25 % for type B material expected at $1800°C$ where $t_{X=50\%}$ is 2.15 time higher. Although this point have high deviation, JMAK kinetics obtained consolidate the mean field approach results.

4 Conclusions

The present article focuses on two main goals: how to analyse the contributions of recrystallization and recovery simultaneously acting in the resulting softening of tungsten during high temperature annealing ($1450°C$ – $1800°C$); how to assess all the parameters involved in the recovery and recrystallization of two types of tungsten in order to understand their differences by a mean field model. The latter predicts the evolution of the radius and the dislocation

density of each grain via interactions with an equivalent homogeneous matrix. Several mechanisms involve for that as for instance, the grain-boundary migration taken into account by the M parameter, or the static recovery characterized by the r parameter.

The second section has dealt with the first aim and has shown how to quantify recrystallization and recovery occurring in the same time by the means of hardness abatement and EBSD. It has clearly confirmed that there is a significant discrepancy between softening kinetics and recrystallization kinetics as claimed by Richou et al [8]. Moreover, the method has been able to quantify the competition between recovery and recrystallization in the two tungsten types and to assess the recovery parameter r and the initial dislocation density in the unrecrystallized grains.

The two types A and B materials have been compared targeting the second aim:

- Their dislocation density in the unrecrystallized grains is at the initial state (delivery) close to $\rho_{A_{def}} = 4.90 \times 10^{13}\,/m^2$ for type A and $\rho_{B_{def}} = 3.02{\times}10^{13}\,/m^2$ for type B. The quite low values are compatible with the fact that both types present some recrystallized grains at this stage so these supplies had undergone at least a final annealing before delivery. Their recovery parameter are similar but varies with temperature as expected. An Arrhenius analysis of thermal activation leads to an apparent activation energy close to $391\,kJ/mol$ for the set A+B.
- Based on EBSD maps collected through this work, initial distributions of deformed grains and nuclei are identified for types A and B materials. Concerning initial recrystallized grains distributions equivalent median (2 % difference) and equivalent standard deviation (19% difference) are obtained for types A and B materials. Concerning initial unrecrystallized grains distributions, higher difference are obtained (48% for the standard deviation).
- Based on the recrystallization fraction (X) and on the softening fraction (X_H) identification , M activation energy was estimated for type A material ($Q_{MA} = 467\,kJ/mol$) and type B materials ($Q_{MB} = 364\,kJ/mol$).

After the completion of this study:

- The predicted kinetics of softening and recrystallization are both reliable.
- The softening and recrystallization kinetics are identified at $1450°C$, $1500°C$, $1550°C$,$1600°C$ and $1500°C$, $1600°C$, $1700°C$, $1800°C$ for types A and B materials respectively. Based on the determination of the apparent M and r activation energies it is now possible to predict the softening and recrystallization kinetics at an uninvestigated temperature.
- The output data leads to explore in a deeper way the competition between softening and recrystallization and then allowed separate softening and recrystallization kinetics. Indeed, calculated kinetics of X_H and X are different. Material softening fraction is always higher than the recrystallization fraction and consequently material can be fully softened while still partially recrystallized.

– To position this work to the literature, softening kinetics obtained by the mean field approach are fitted by the use of JMAK model. Parameters are now available. Comparison with JMAK kinetics fitted on the experimental points are made in the discussion and revealed that kinetics are quantitatively comparable regarding the time to reach 50% softening which consolidates the mean field approach results.

Once assessed the parameters for types A and B, the mean field model is now ready to assess the effect of mobility and recovery activation energies, dislocation density and grain size distributions at initial state on the softening and recrystallization processes during annealing treatment.

For further works, the present model could be used in the following to define the ideal tungsten microstructure and optimize the tungsten armoured plasma facing component lifetime.

5 Acknowledgements

This work has been carried out within the framework of the contract IO/CT/18/4300001734 with ITER Organization. The views and opinions expressed herein do not necessarily reflect those of the ITER Organization.

The authors express their deep gratitude to G. De Temmerman from ITER Organization for its support and deeply acknowledge Marilyne Mondon and Gilles Blanc from Mines Saint-Etienne for their help in sample preparation.

Appendix A: computational information

Serial Pyhton environment have been used to develop the mean field model. The average computational time for numerical annealing simulations (including the optimization loop to estimate the M parameter) is equal to 2 minutes (Intel(R) Core(TM) i7-10875H CPU @ 2.30GHz / RAM Memory 32.0 Go).

Appendix B: Validation of the mean field kinetics based on a comparison with the JMAK kinetics

JMAK kinetics are used to compare results from the mean field model. Proposing an unified description of recovery/recrystallization mechanisms, the JMAK model defines the X_h evolution over the annealing time as follow (equation 24) [6]:

$$X_h = 1 - \exp(-(b^n(t + t_{eqh})^n) \tag{24}$$

Three parameters are introduced: n corresponding to the Avrami exponent, b which is a thermo-dependent parameter and t_{eqh} which was introduced to assume an equivalent holding time to take into account the non-zero softening fraction at t=0.

type A	b	n	$t_{eqh}(s)$
$1450°C$	1.27×10^{-4}	2.36	3700
$1500°C$	4.57×10^{-4}	1.05	400
$1550°C$	5.34×10^{-4}	3.00	1035
$1600°C$	1.88×10^{-3}	3.00	293
type B			
$1500°C$	1.88×10^{-4}	3.00	2165
$1600°C$	8.56×10^{-3}	3.00	500
$1700°C$	3.50×10^{-3}	1.69	60
$1800°C$	1.10×10^{-2}	2.86	34

Table 7 JMAK parameters related to JMAK_exp obtained for types A and B materials

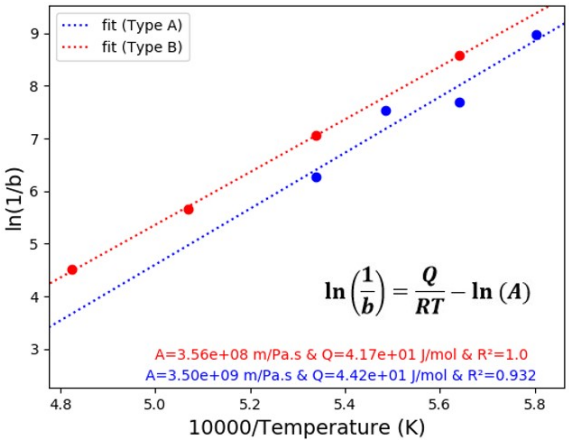

Fig. 16 Arrhenius plot of the JMAK parameter b for types A and B materials related to the JMAK_exp kinetics.

Conflict Of Interest

A. Durif, D.Piot, M. Richou, L.Gallais, M. Lemetais, M.Lenci, M. Minissale, G.Kermouche declare have received financial support and tungsten materials from ITER Organization.

References

1. ITER Structural design criteria for in-vessel components (SDC-IC) appendix A: Materials design limit data , g74ma, 8 01-05-28w0.2, 2013
2. Pintsuk, G. (2012). 4.17 - tungsten as a plasma-facing material. In Konings, R. J., editor, Comprehensive Nuclear Materials, pages 551 581. Elsevier, Oxford.
3. S.Nogami et al, Mechanical properties of tungsten: Recent research on modified tungsten materials in Japan, Journal of Nuclear Materials 543 (2021) 152506
4. T. Pütterich et al, Calculation and experimental test of the cooling factor of tungsten, Nuclear Fusion 50(2):025012 (2010).
5. S. Panayotis, et al, Self-castellation of tungsten monoblock under high heat flux loading and impact of material properties. Nuclear Materials and Energy, 12 :200 204. Proceedings of the 22nd International Conference on Plasma Surface Interactions 2016, 22nd PSI.

6. F.J. Humphreys and M.Hatherly (2004). Recrystallization and related annealing phenomena (second edition)
7. A.Alfonso et al. Recrystallization kinetics of warm-rolled tungsten in the temperature range 1150–1350 C, Journal of Nuclear Materials 455 (2014) 591–594
8. M. Richou et al, Recrystallization at high temperature of two tungsten materials complying with the ITER specifications, Journal of Nuclear Materials 542 (2020) 152418
9. W.A. Johnson and R.F. Mehl, "Reaction kinetics in process of nucleation and growth" . Trans. AIME, 135, p. 416-458 (1939). 28
10. M.Avrami, Kinetics of phase change. I: General theory. II: Transformation time relations for random distribution of nuclei. III: Granulation, phase change and microstructure. J. Chem. Phys., 7, p. 1103-1112 (1939) ; 8, p. 212-224 (1940) ; 9, p. 177-184 (1941).
11. V. Shah et al, Recrystallization behaviour of high-flux hydrogen plasma exposed tungsten, Journal of Nuclear Materials, Vol 545, 2021, 152748
12. A.Durif et al, Inverse identification of tungsten static recrystallization kinetics under high thermal flux, Fusion Engineering and Design, Vol 146, Part B, September 2019, Pages 1759-1763
13. D. Srolovitz, et al., 1983. Grain growth in two dimensions. Scripta Metallurgica, 17(2), pp.241–246
14. A. Alfonso et al .Thermal stability of a highly-deformed warm-rolled tungsten plate in the temperature range $1100 - 1250°C$, Fusion Engineering and Design 98–99 (2015) 1924–1928
15. Umberto M.Ciucani et al, Recovery and recrystallization kinetics of differently rolled, thin tungsten plates in the temperature range from $1325°C$ to $1400°C$, Nuclear Material and Energy 20 (2019) 100701
16. K. Wang et al, Recrystallization behavior of pure tungsten hot-rolled with high accumulated strain during annealing at $1250 - 1325°C$, Materials Science & Engineering A 806 (2021) 140828
17. M. Minisale et al, A high power laser facility to conduct annealing tests at high temperature Review of Scientific Instruments 91, 035102 (2020)
18. Y.B. Chun et al, 2006. Monte Carlo modeling of microstructure evolution during the static recrystallization of cold-rolled, commercial-purity titanium. Acta Materialia, 54(14), pp.3673–3689.
19. Raabe, D., 1999. Introduction of a scalable three-dimensional cellular automaton with a probabilistic switching rule for the discrete mesoscale simulation of recrystallization phenomena. Philosophical Magazine, 79(10), pp.2339–2358.
20. S. Sahay et al, 2009. Modeling the topological features during grain growth by cellular automaton. Computational Materials Science, 46(1), pp.92–99.
21. Miodownik, M.A., 2002. A review of microstructural computer models used to simulate grain growth and recrystallisation in aluminium alloys. Journal of Light Metals, 2(3), pp.125–135.
22. Fan, D. & Chen, L.Q., 1997. Computer simulation of grain growth using a continuum field model. Acta Materialia, 45, pp.611–622.
23. Bernacki, M. et al., 2009. Finite element model of primary recrystallization in polycrystalline aggregates using a level set framework. Modelling and Simulation in Materials Science and Engineering, 17(6), p.064006.
24. Montheillet, F., Lurdos, O. & Damamme, G., 2009. A grain scale approach for modeling steady-state discontinuous dynamic recrystallization. Acta Materialia, 57(5), pp.1602–1612.
25. Bernard, P. et al., 2011. A two-site mean field model of discontinuous dynamic recrystallization. Materials Science and Engineering A-Structural Materials Properties Microstructure and Processing, 528(24), pp.7357–7367.
26. A. Mannheim et al, Modelling recrystallization and grain growth of tungsten induces by neutron displacement defects, Mechanics of Materials 123 (2018) 43-58
27. A Mannheim et al, 2019 Modelling Simul. Mater. Sci. Eng. 27 065001
28. G. Smagghe et al, "The Issue of Grain Size Distribution Using Mean Field Models for Dynamic and Post-Dynamic Recrystallization", Materials Science Forum, Volume 879, 2017, pp 1794-1799

29. D. Piot et al, "A semitopological mean-field model of discontinuous dynamic recrystallization: Towards a correct and rapid prediction of grain-size distribution", Journal of Materials Science, 53, 2018, pp 8554-8566.
30. Tabor D., The hardness of metals, 1951 , Oxford Claredon press, Oxford
31. X. Hu et al, Irradiation hardening of pure tungsten exposed to neutron irradiation, Journal of Nuclear Materials 480 (2016) 235-243
32. D.Terentyev et al, Synergy of plastic deformation and gas retention in tungsten, Nucl. Fusion 55 (2015) 013007 (5pp)
33. K. Wang et al, Effects of thickness reduction on recrystallization process of warm-rolled pure tungsten plates at $1350°C$, Fusion engineering and Design, Vol 125, 2017, Pages 521 - 525